# Can a laboratory experiment express the size effect on the drying of refractory castables?

M. H. Moreira[a,*], H. Peng[c], S. Dal Pont[b], V. C. Pandolfelli[a]

[a] *Federal University of Sao Carlos, Graduate Program in Materials Science and Engineering (PPGCEM), Rod. Washington Luiz, km 235, 13565-905, São Carlos, SP, Brazil*

[b] *Université Grenoble Alpes, CNRS, Grenoble INP, 3SR, 38000 Grenoble, France*

[c] *Materials Innovation, Elkem Silicon Products Development, Kristiansand, Norway*

**Abstract**

Refractories play an important role in societies' progress as they enable extensively consumed materials to be processed such as steel and cement. Because of the high demand of these supplies, refractory-lined equipment comprises massive structures that have large dimensions and weighs several tons. Conversely, laboratory samples, used to study the behavior of these materials, are orders of magnitude smaller and often found weighing less than 1kg. Within the context of refractory castable drying, this work aims to investigate the impact of size effects on water removal dynamics during thermogravimetry tests. The analysis of mass loss and its derivative with respect to temperature indicates that increasing the heating rate applied in the small samples can lead to a better reproduction of the evaporation and ebullition stages of the drying of large ones, due to the compensation effect of the faster temperature increase on the smaller sample sizes leading to similar thermal gradients.

*Corresponding Author

*Email address:* murilo.moreira@estudante.ufscar.br (M. H. Moreira)

Furthermore, the presence of polymeric fibers and their influence on the size effect are also examined, showing that the increased permeability induced by such additives reduces the intensity of the scale effect. Additionally, it was found that for cubic samples with sizes equal to or larger than 10cm, a kink in the temperature evolution measured at the center of the samples took place. A hypothesis based on the results and on observations of recent studies is proposed to explain this phenomenon, attributing it to the rapid evaporation of accumulated liquid water at those positions. This study also highlights the importance of considering the size-dependent nature of drying dynamics in refractory castables, as conventional thermogravimetry on laboratory scale samples may overlook important phenomena. Understanding the mechanisms occurring at real structural scales during water removal is crucial for predicting their behavior upon heating and enabling faster and safer drying processes for refractories.
*Keywords:* Refractory Castable, Drying, Scale Effect, Thermogravimetry, Polymeric Fibers

---

## 1. Introduction

Refractory materials are required for the high temperature processes involved in the production of steel and cement, which are currently the two most consumed materials in the world [1].

The sheer volume of production demand of these products is related to the increase of the equipment sizes (such as blast furnaces, converters, steel ladles, tundishes, etc.) able to provide the required scale of the output, which also leads the refractories to sustain large mechanical loads and multiaxial

stress conditions [2].

Hydraulic-bonded castables is one of the most broadly used types of monolithic refractories in such applications [3] and their green mechanical strength derives by the hydration reactions of its binders [4, 5]. Calcium aluminate cement, also referred to as CAC, presents several desired features, such as high refractoriness, fast curing and rapid development of high green strength, as well as corrosion resistance under certain conditions [4]. One of the largest drawbacks of these materials, however, is during their first heating up to the working temperature.

This challenge is related to the high density and low permeability of the resulting microstructure of CAC-containing compositions, which was itself a consequence of extensive development efforts to design particle packing models to maximize the density and minimize the porosity [5]. However, an unintended consequence emerged, as these compositions are more prone to explosive spalling during the drying stage [5].

This phenomenon is characterized by the sudden release of stored potential energy leading to crack propagation through the material, causing substantial damage to the refractory lining and requiring its replacement in critical situations. Similar issues can be found for Portland cement concrete structures under fire [6]. Recent theories elucidating the mechanism behind explosive spalling attribute it to a combination of water vapor pressurization (generated from the evaporation of non-reacted water and from the dehydration [7]) and thermomechanical stresses [7, 8, 9].

Consequentially, the strength of the refractory castable plays a crucial role in such accidents [7, 8]. This property, however, is known to be affected

by the size of the body itself, a feature that is particularly significant when considering the large industrial structures lined with refractory castables.

This size effect is observed when there is a deviation from the scaling theory of strength [10]. There are two reasons for this behavior: first, defects acting as stress concentrators during the loading of the structure are randomly distributed within the samples giving rise to what is known as "statistical size effects". Thus, smaller samples present a lower probability of having a larger critical defect that will lead to the local stress to overcome the material's mechanical strength, for a given applied load [11]. The second reason is linked to the toughening mechanisms of dissipation of energy without increasing the main crack's length, which is called the "energetic size effect" [10].

When considering the accidents observed during the drying stage of refractory castables, these aspects are crucial for interpreting laboratory tests and extrapolation to industrial scale bodies, as a smaller volume cannot reproduce the mechanical responses of a larger one. Therefore, the presence or lack of explosive spalling during the drying of a refractory castable lining cannot be guaranteed to align with the findings observed in laboratory experiments, even if the applied conditions (temperature increase schedule, heaters' location, boundary conditions, etc) are similar.

In this context, besides the size effect on the mechanical behavior, Alarcon-Ruiz et al. [12] have also demonstrated that the volume of a sample can lead to changes in the measurements of intrinsic permeability of Portland cement concrete samples. This finding also poses questions on the representativeness of laboratory scale measurements to understand large systems [12], and

it questions whether permeability itself can be stated as an intrinsic property.

The size of a sample has another significant impact on the dynamics of mass transfer within a porous medium, specifically regarding the surface area to volume ratio ($S_a/V$). It is broadly known that, for a given geometry, as the size of the sample increases, the surface area to volume ratio decreases. This reduction in surface area relative to the volume, affects the drying process as mass is primarily released through the external surfaces of the sample. Consequently, larger samples experience hindered drying due to their lower surface area compared to their volume.

This phenomenon can be also understood by considering the spray-drying method, as an example, where, the smaller droplets, with a large surface area to volume ratio, will preferably undergo rapid water removal [13]. Additionally, Cardoso et al. demonstrated that for cylindrical samples of refractory castables with equal diameter and height, as well as distinct sizes ranging from 1.7cm to 5.2cm, the likelihood of facing explosive spalling in lab tests increased, due to both an increase on the path for the water at the innermost positions to reach the ambient environment, as well as the reduction of the surface area to volume ratio [14].

Lastly, as the drying of refractory castables is non-isothermal, the heat transfer behavior also plays a crucial role. It is well-established that bodies with different volumes will exhibit distinct heat transport dynamics. This can be quantitatively evaluated by considering the Fourier number, Fo, as defined in Equation 1.

$$\mathrm{Fo} = \frac{\alpha t}{L^2} \tag{1}$$

where $\alpha$ is the material's thermal diffusivity, $t$ is time and $L$ is the characteristic length through which thermal conduction occurs.

For the same refractory castable composition and the same time period (that is, fixing $\alpha$ and $t$ in Equation 1), the larger the body ($L$), the smaller the resulting Fourier number. This means that during heating of one of its surfaces, for instance, a significant temperature increase can only be observed in a small region next to the heated boundary, yielding large temperature gradients. Consequently, longer times are needed to reach a stationary state [15]. Thus, the increase in size of a given sample will have a direct impact on its thermal state, even if the same heating curve is applied during the drying of bodies with distinct sizes.

As the water removal stages are defined by the current temperature, this thermal size effect will have a great impact on drying. Moreover, the thermal stresses developed within the sample will be directly affected by this different temperature distribution, and thus the explosive spalling likelihood scales with the size of the bodies.

These effects can be exemplified by the different ways that a material can undergo explosive spalling. In the context of drying large industrial equipment lined with refractory castables, an explosion thrusts large pieces of the lining over long distances [9]. Meanwhile, for Portland cement reinforced concrete structures, this process occurs by a successive spalling of layers of the body, as described by Jansson et al. [6]. In laboratory scale thermogravimetry tests under high heating rates (also known as "explosion tests"), yet another mode of failure is observed as the complete destruction of the sample in small pieces takes place [4, 5, 9].

Due to the lack of comprehensive size effect studies on the refractory research area, previous experiences on fire accidents of Portland cement concrete could shed some light on this issue. Overall, no single simplified rule could be disclosed. Connolly et al. studied the effect of different thickness on the spalling of samples under distinct loading conditions [16], and concluded that when the sample was subjected to mechanical loads, the likelihood of a more severe explosive spalling taking place increased. It was also found that thinner slabs of concrete (50mm) were more prone to spalling than thicker ones (100mm), as the damage on the former was observed even when much lower mechanical loading was applied [16]. The proposed explanation to this was that the thinner sections heated faster, leading to higher vapor pressures and more intense explosive spalling. Jansson and colleagues reported that small slabs (600 x 500 x 200 $mm^3$) with the same thickness as larger ones (1800 x 1200 x 200 $mm^3$) spalled considerably less when both samples were subject to the same load [17].

Kodur et al. suggested that the risk of explosive spalling increased with the specimen size [18]. Such a claim was supported by different experimental observations as the ones reported by Boström et al. which revealed that even though the percentage of weight loss of large (1800 x 1200 x 400 $mm^3$) and small slabs (400 x 400 x 100 $mm^3$) were comparable, the spalling depth was much smaller for the ones with a smaller volume [19]. The authors attributed this to the fact that water and vapor could escape more easily in smaller slabs, decreasing the likelihood and amount of spalling.

Proposing to directly study the size effect, Mohd Ali et al. tested large (3380 x 3360 x 200 $mm^3$) and medium slabs (1075 x 1075 x 200 $mm^3$),

a column (1000 x 400 x 400 $mm^3$), and cylinders (200 mm high x 100 mm diameter) during direct heating of the bodies [20]. The results in terms of the nominal spalling depth (calculated as the total volume loss of the specimen divided by its exposed area, in order to compare the different geometries) suggested that as the specimen size increases, so does the spalling of concrete [20]. Besides, it was found that "beyond a certain thickness of a panel, the thickness has very little effect on the spalling of the exposed surface". Finally, the authors also linked this volume correlation with the spalling depth to the fact that explosive spalling is a fracture process mechanism which is associated to the energetic and statistical size effects described by Bažant et al. [10].

Finally, more recently, Sultangaliyeva et al. analyzed the mean and maximum depth of spalling for three different geometries: i) prisms of 20 x 20 x 10 $cm^3$, ii) slabs of 100 x 170 x 30 $cm^3$ and iii) large hollow cubes of 202 x 202 x 165 $cm^3$, all subject to the same ISO 834-1 fire curve [21]. It was observed that the spalling depth increased with the volume of the sample [21]. The authors also confirmed the findings of previous studies that when external loads were applied, the explosive spalling was more intense [21].

All these efforts share a common objective of investigating the response of concrete structures at high temperatures within the context of fire accidents. Accordingly, they concentrated on examining the size effect on the occurrence of explosive spalling through tests designed to simulate the rapid heating that reproduced the fast dynamic typically encountered in fires. Additionally, the observations were carried out a posteriori, i.e. based on measurements after testing, which overlooked the dynamic behavior of the water removal process.

Lastly, an additional aspect that was not taken into account in these studies is the likely correlation that might exist between the scale effects and using additives that directly affect the water transport within the concrete, such as polymeric fibers. These additives are commonly incorporated to enhance the fire resistance of cement containing structures and also act as drying agents for refractory castables. The understanding of their effect on the water removal is often based on laboratory scale samples, consequently, hiding the role that likely size effects have on such compositions is crucial for providing insights on their mechanisms and most importantly optimizing their performance.

Thus, the objective of the current study is to investigate the size effect on the dynamics of water removal during the drying of refractory castables through the macro thermogravimetry analysis (TGA) originally proposed by Peng et al. [22]. This technique enables the examination of samples weighing up to 80 kg, enabling a comprehensive assessment of thermal evolution, mass loss, and their derivatives for refractory castable compositions of varying sizes. Additionally, the present work will consider the effect of distinct heating rates and the presence or absence of polymeric fibers in the compositions. Thus, it is expected that the current findings will help to bridge the gap between laboratory analysis and industrial drying processes, while also providing a more in-depth understanding of the drying mechanisms that take place in refractory castables at high temperatures.

## 2. Material and Methods

### *2.1. Refractory Castable Composition and Processing*

Two high alumina free-flowing castable compositions were considered in the present work, one without the addition of any drying additive (5CAC), which was the reference for the study and another one named 5CAC-ED containing polymeric fibers (EMSIL Dry, Elkem, Norway). Both compositions were formulated based on Andreasen's particle packing model, considering a distribution coefficient $q = 0.21$.

The primary distinction between the two compositions, apart from the fiber addition, was the water content (5 wt.% for 5CAC and 5.25 wt.% for 5CAC-ED). The castable containing the drying additives required a slightly higher water content to guarantee the raw material homogenization and suitable flowability for the processing of the castables, due to the presence of fibers. The complete compositions for both castables are described in Table 1.

Table 1: High-alumina refractory castable compositions studied in this work.

| Raw Materials | | Composition (wt.%) 5CAC | 5CAC-ED |
|---|---|---|---|
| Tabular alumina | AT 6-3 (Almatis, Germany) | 18 | 18 |
| | AT 3-1 (Almatis, Germany) | 10 | 10 |
| | AT 1-0.5 (Almatis, Germany) | 11 | 11 |
| | AT 0.6-0.2 (Almatis, Germany) | 9 | 9 |
| | AT 0.2-0 (Almatis, Germany) | 16 | 16 |
| | AT $< 45$ (Almatis, Germany) | 10 | 10 |
| Calcined and reactive alumina | CL370 (Almatis, Germany) | 11 | 11 |
| | CT3000SG (Almatis, Germany) | 10 | 10 |
| Aluminate Cement | Secar 71 (Imerys Aluminate, France) | 5 | 5 |
| Polymeric Fiber | EMSIL Dry (Elkem, Norway) | - | 0.1 |
| Water | Distilled water | 5 | 5.25 |
| Dispersant | Castament FS60 (BASF, Germany) | 0.2 | 0.2 |

The powders were pre-mixed for one minute, and then the water content was gradually added over the course of three minutes. Following that, the samples were cast into molds to obtain the geometries and volumes shown in Figure 1. The samples were cured at room temperature in plastic bags containing beakers filled with water. This ensured that the environment inside the bags was humid during the 24-hour curing period.

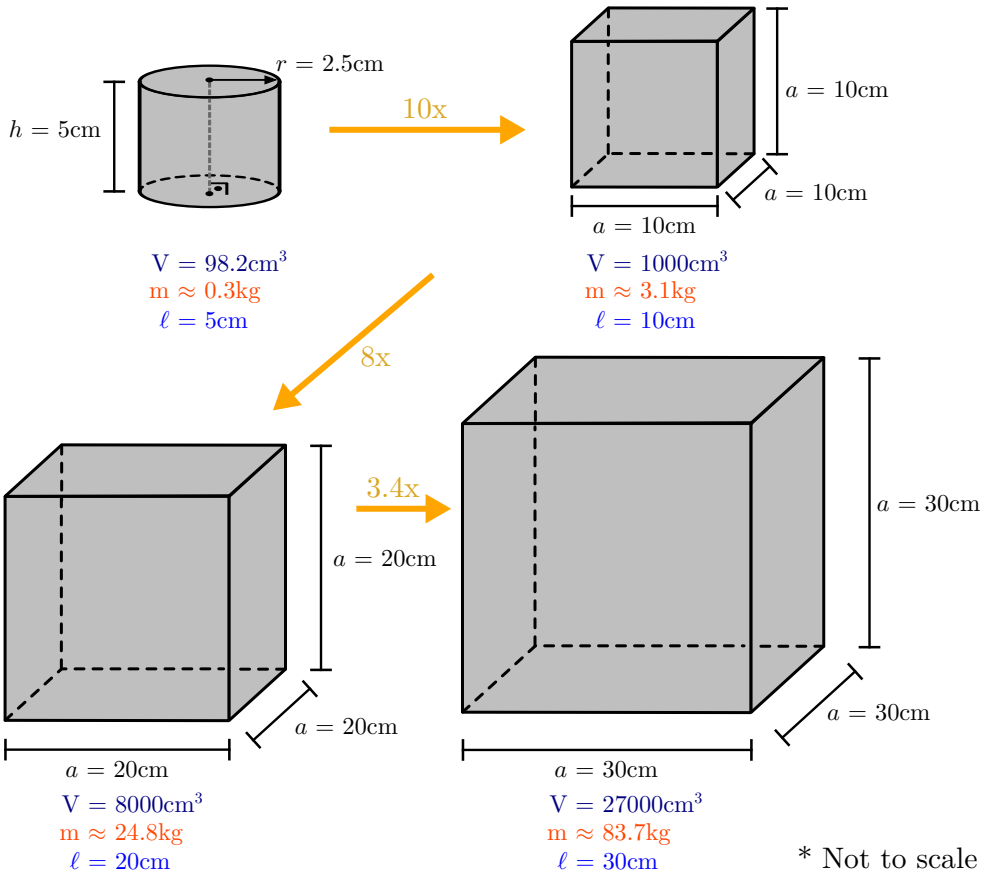


Figure 1: Volumes, masses and characteristic lengths of the samples tested in the present work.

### *2.2. Thermogravimetry Analysys (TGA)*

Castable samples were tested following the experimental design shown in Table 2. A total of three parameters were considered: i) the presence of polymeric fibers in the composition, ii) the heating rate applied during the TGA test, and, finally, iii) the characteristic length (which also implied in changes of the TGA equipment, on the shape of the sample and on the surface area to volume ratio).

Table 2: Experimental design followed in the current work.

| Test | TGA Equipment | Heating Rate | Composition | Shape | Characteristic Length, $\ell$ | Surface Area to Volume Ratio, $S_a/V$ |
|---|---|---|---|---|---|---|
| 1 | Macro TGA | 0.83°C/min | 5CAC | Cube | 30cm | 20 $cm^{-1}$ |
| 2 | Macro TGA | 0.83°C/min | 5CAC | Cube | 20cm | 30 $cm^{-1}$ |
| 3 | Macro TGA | 0.83°C/min | 5CAC | Cube | 10cm | 60 $cm^{-1}$ |
| 4 | Conventional | 2°C/min | 5CAC | Cylinder | 5cm | 120 $cm^{-1}$ |
| 5 | Conventional | 5°C/min | 5CAC | Cylinder | 5cm | 120 $cm^{-1}$ |
| 6 | Conventional | 20°C/min | 5CAC | Cylinder | 5cm | 120 $cm^{-1}$ |
| 7 | Macro TGA | 0.83°C/min | 5CAC-ED | Cube | 30cm | 20 $cm^{-1}$ |
| 8 | Macro TGA | 0.83°C/min | 5CAC-ED | Cube | 20cm | 30 $cm^{-1}$ |
| 9 | Macro TGA | 0.83°C/min | 5CAC-ED | Cube | 10cm | 60 $cm^{-1}$ |
| 10 | Conventional | 2°C/min | 5CAC-ED | Cylinder | 5cm | 120 $cm^{-1}$ |
| 11 | Conventional | 5°C/min | 5CAC-ED | Cylinder | 5cm | 120 $cm^{-1}$ |
| 12 | Conventional | 20°C/min | 5CAC-ED | Cylinder | 5cm | 120 $cm^{-1}$ |

Macro TGA (MTGA) tests were specifically selected to include samples with a minimum characteristic length, $\ell$, of 10 cm, corresponding to a weight of approximately 3 kg. This choice was made because the equipment was initially designed for handling larger samples weighing up to 80 kg. However, during the experimental part, it was found out that the setup was not as precise for obtaining reliable mass readings even for the $\ell = 10$cm samples due to excessive noise in the signal output. Despite this limitation, the temperature readings obtained for these tests yielded valuable results, which are presented in this study.

The heating rate of the Macro TGA was also restricted to 0.83°C/min due to the significant risk associated with the explosive spalling of such large samples. Furthermore, all the MTGA samples had a cubic geometry, and as their dimensions decreased, the surface area to volume ratio, $S_a/V$, increased as shown in Table 2.

Conversely, the conventional tests (CTGA) were limited to cylindrical samples with 5cm in diameter and 5cm in height, due to the size of the fur-

nace's internal chamber [5]. These dimensions yielded to the largest surface area to volume ratio in the experimental plan. As the sample geometries and sizes could not be changed for the conventional test layout, the heating rate applied in such tests was varied, as it was expected that this would induce different levels of thermal gradients within the samples. This effect can be readily identified when considering the Fourier's number (Fo) calculation for the heating of the center of each sample by 1°C, as shown in Figure 2. This procedure is the same as fixing the time $t$ in Equation 1 to the reciprocal of the heating rate applied for each specific test.

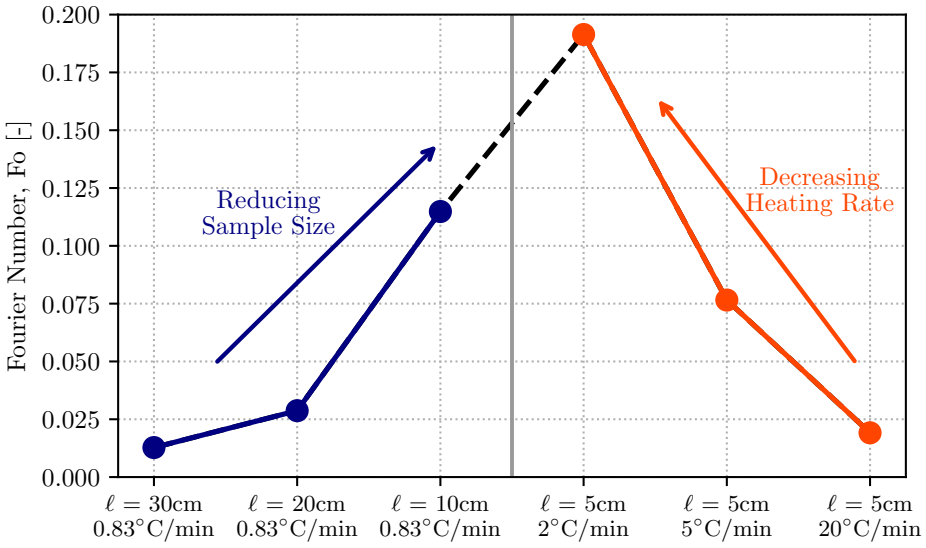


Figure 2: Fourier's numbers calculated for the increase of 1°C at the center of the sample for the tests considered in the experimental design. Results in blue are the ones obtained for the macro TGA equipment whereas the ones in red are those for the conventional test.

The Fourier number is inversely proportional to the thermal gradients that are developed during the heating of a given body [15]. As such, reducing the sample size for the MTGA samples, or decreasing the heating

rate applied to the CTGA tests, results in a higher Fourier number, which will correspond to the smaller thermal gradients within the samples. Consequently, it is expected that increasing the heating rate may lead to thermal states much closer to those observed for larger samples. This proposition was also investigated in the current experimental plan.

The layout of the MTGA and CTGA tests is presented in Figure 3. The main difference between the equipment, aside from their size, is the location of the heating elements. For the conventional setup, the heaters are placed on both sizes of the sample, whereas for the macro TGA, its heating elements are located at the bottom of the sample. Tests with thermocouples placed at different positions within the furnaces' chambers showed that the temperature differences at distinct positions inside the heating chamber were 30°C at most for the MTGA and 15°C for the CTGA. Both systems comprised a cage to protect the furnaces from sample explosions.

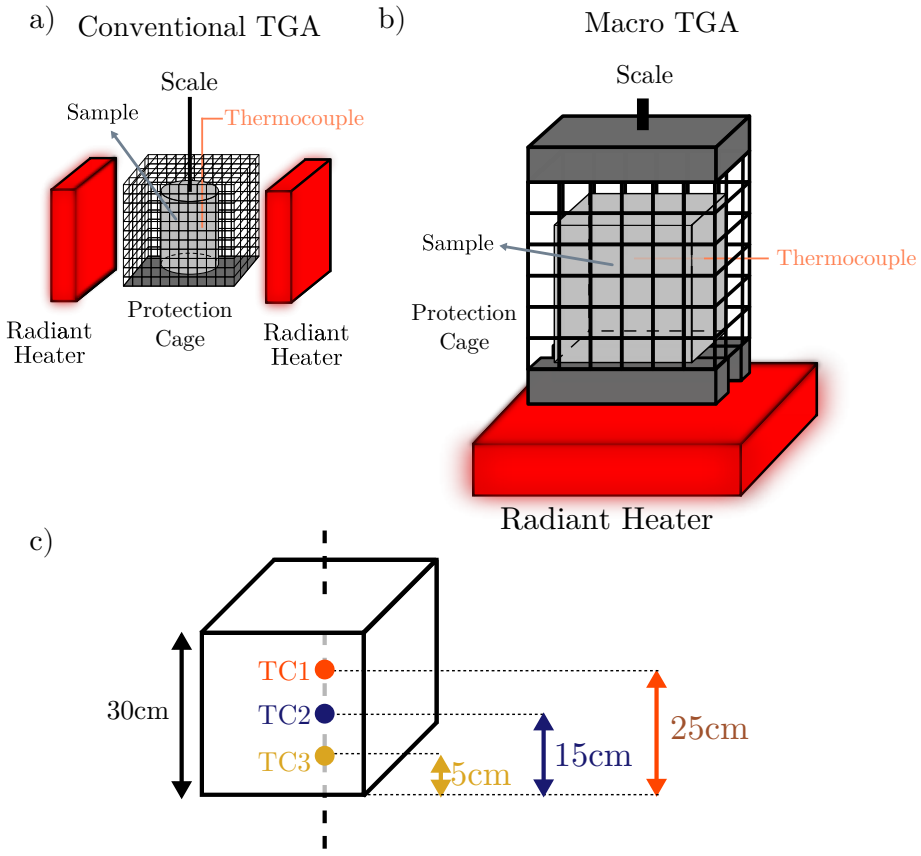


Figure 3: Experimental layout for (a) the conventional thermogravimetry equipment, (b) the macro TGA equipment and the location of the thermocouples inside the samples with characteristic length $\ell = 30$cm.

Finally, the tests conducted with the $\ell = 30$cm samples comprised three thermocouples located at different heights along the central axis of the sample. These were designated as TC3 (placed closer to the bottom, h=5cm), TC2 (in the middle, h=15cm) and TC1 (close to the top h=25cm) as described in Figure 3 c). For the test with the composition without fibers, the thermocouple TC3 at the bottom of the sample failed to register the temperature during the experiment. As a result, the analysis for this particular test

only considered the temperature measurements recorded by the top (TC1) and middle (TC2) thermocouples. For the other cubic and cylindrical sample geometries, a single thermocouple was placed at the sample center to record the temperature changes during the heating process.

The mass curves profiles obtained from the MTGA and CTGA experiments were normalized by the initial value as described in Equation 2, providing a relative comparison of mass changes over time for samples with different sizes. Meanwhile, the derivative of the normalized mass with respect to the sample temperature was obtained following the central finite difference approximation, which involves subtracting the normalized mass values and temperatures at adjacent time points to obtain the numerical derivative. This is described by Equation 3.

$$W_i = 100 \left( \frac{M_0 - M_i}{M_0 - M_f} \right) \tag{2}$$

where $W_i$ is the normalized mass at time $t_i$, $M_0$ is the initial mass at $t_0 = 0s$, and $M_f$ is the value at the end of the test.

$$\left( \frac{\partial W}{\partial T} \right)_i = \frac{W_{i+1} - W_{i-1}}{T^s_{i+1} - T^s_{i-1}} \tag{3}$$

where $W_{i+1}$ and $T^s_{i+1}$ are the mass and the temperature at the center of the sample for the time $t_{i+1}$, and, $W_{i-1}$ and $T^s_{i-1}$ are such values at an earlier moment $t_{i-1}$.

## 3. Results and Discussions

The initial set of results analyzed in the current work refers to the temperature evolution at the center of the sample, presented in Figure 4. Because of the different heating rates for the CTGA and MTGA tests, the results are organized in graphs in which the vertical axis represents the same temperature range for all tests, whereas the horizontal axis represents different time ranges.

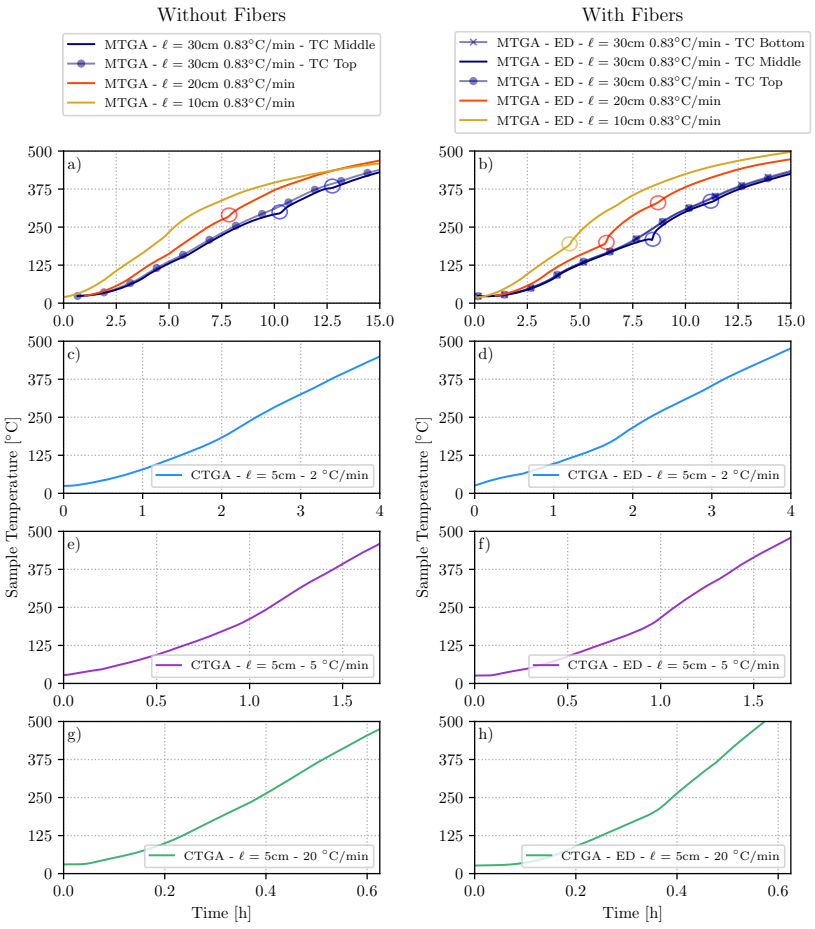


Figure 4: Temperature evolution for the samples without (left column) or with polymeric fibers (right column). The time scale at the x-axis is different because of the distinct heating rates applied.

Figure 4 a) shows the macro TGA results for the reference compositions (without polymeric fibers) with a heating rate of 0.83°C/min. Notably, the heating of the sample with characteristic length $\ell = 10$cm shows a clear change in the slope of the temperature evolution around 5h at 250°C. Comparatively, the larger samples display a change in slope at higher temperatures (around 270°C) and are preceded by sharp kinks in the heating curve

(referred to as "thermal kinks"). Furthermore, the largest sample ($\ell = 30$ cm) exhibits a secondary thermal kink at 375°C. Interestingly, the phenomenon is only observed for the thermocouple positioned at the middle of the sample, whereas the results for the top one do not show this behavior.

Figure 4 b) presents the MTGA results for the samples containing polymeric fibers. In this case, thermal kinks were also found even for the $\ell = 10$cm MTGA sample, albeit less significant. The intensity of the event was directly proportional to the samples' size, whereas the temperature at which the process took place remained approximately the same, at around 225°C. It should be noted that this is nearly 50°C lower than the temperature in which the thermal kinks were observed for the tests with the reference composition. This behavior was again not detected for the top nor for the bottom thermocouples, whereas a secondary kink could be detected for the larger samples ($\ell = 20$cm and $\ell = 30$cm) at higher temperatures, around 350 °C.

For the conventional TGA tests, Figures 4 (c-h), no kinks were observed and only minor changes in the heating slope were present. Moreover, this slope change was also less intense for the reference compositions without polymeric fibers.

Thus, it can be concluded so far that the occurrence of the thermal kink is associated to the sample size and the position of the thermocouple within the sample. To gain a better understanding of the dynamics of this phenomenon, the sample without fiber and with a characteristic length $\ell = 30$cm was selected for a more detailed analysis in Figure 5.

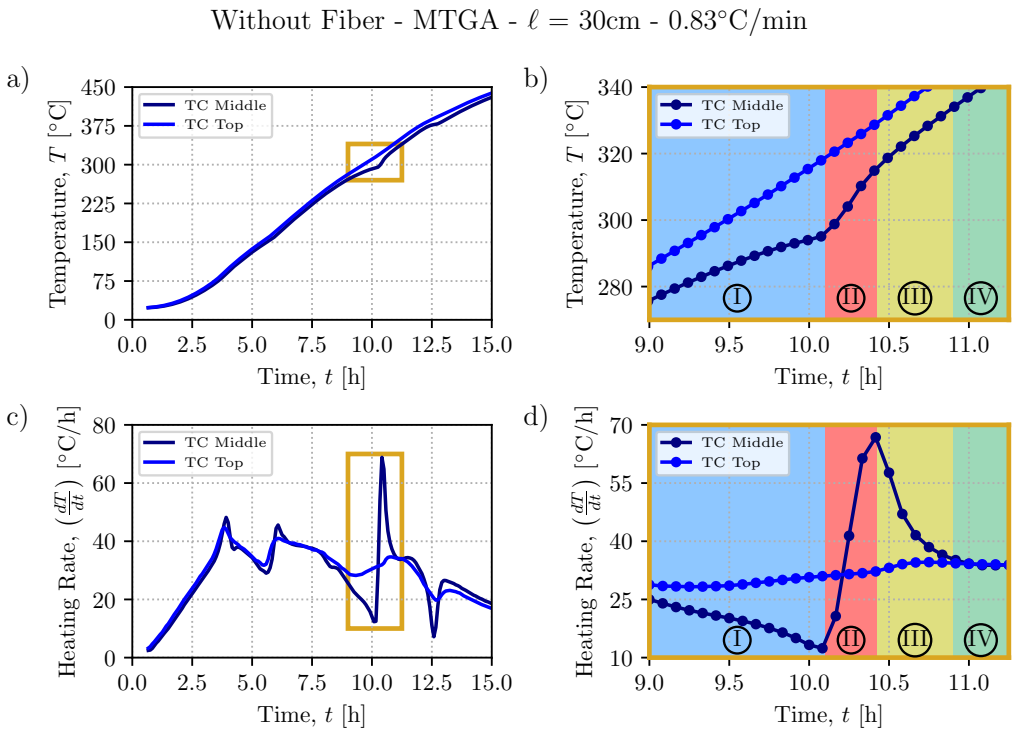


Figure 5: Detailed view of the largest kink on the temperature for the samples $\ell = 30$cm without polymeric fibers. In (a), the overall temperature profile is described, (b) is the zoomed region identified in (a) as the dark yellow rectangle. In (c), the heating rate is plotted and (d) depicts the zoomed region in dark yellow.

Upon closer examination, the first difference in the thermal evolution between the middle and top positions (highlighted in dark yellow in Figure 5 a) can be identified between 9h and 11h when the temperature varies from 270°C to 340 °C. Figure 5 b) provides a zoomed view of this region, where four distinct stages are highlighted in blue, red, yellow and green.

The first stage, I, displays a decrease in the heating rate. This can be quantified by the derivative of the temperature with respect to time depicted in Figure 5 c), where, as expected, the temperature results for the thermocouples at the middle and the top are roughly the same from the beginning

of the test up to the 9-hour mark. From the zoomed region shown in Figure 5 d), one can see a drop in the heating rate calculated for the TC Middle, decreasing from 25°C/min at the 9-hour mark to a minimum of 10°C/min at 10.1 hours.

From that point, the second stage, II, begins where a steep increase in the heating rate at TC takes place in just under 20 minutes, reaching 70°C/min. Stage III follows with a decrease in the heating rate until it reaches the one observed at TC-Top, which is closely followed during the last stage, IV.

This rapid changing heating behavior suggests that the local thermal properties around the thermocouple at the middle of the sample are significantly changing in a short period compared to the total test duration. To further investigate the potential causes for these steep changes, Figure 6 highlights the heating and mass loss rates evolution for the samples both with and without polymeric fibers, considering $\ell = 30$ cm.

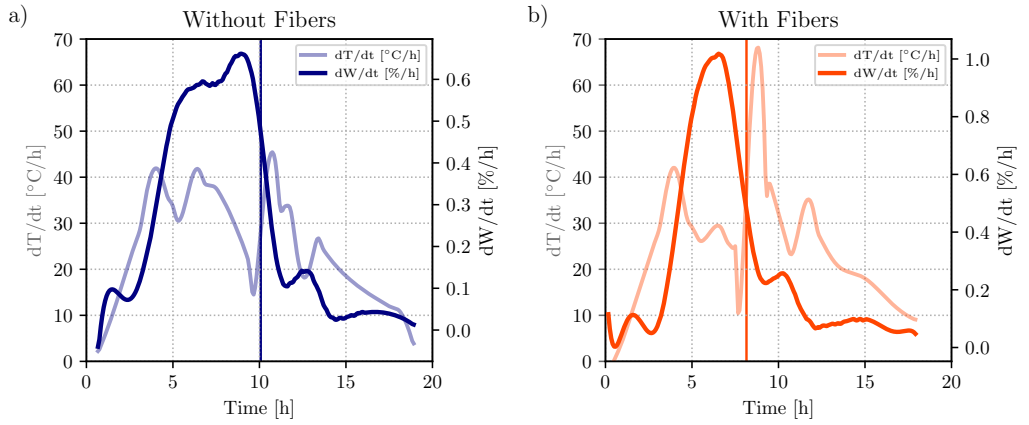


Figure 6: Temperature derivative and mass loss rate evolution, both versus time for the samples $\ell = 30$cm without (a) or with polymeric fibers (b). The time for the largest kinks on the temperature increase curves are highlighted with vertical lines.

The time when the first and largest thermal kink takes place is identified through a vertical line in both Figures 6 a) and 6 b). It can be noted that for both compositions at such moments, the thermal kink occurs right after the peak of mass loss rate. Moreover, the addition of polymeric fibers resulted in a shift of the water removal rate peak to lower temperatures. This relationship between the thermal variation and the decrease of mass loss rate is also evident for the secondary thermal kinks, which take place around 12.5h for the reference composition and around 11.5h for 5CAC-ED.

This suggests a strong correlation between the variation of local thermal properties and the dynamics of the water removal. As this process is highly affected by the drying additives, it shifts both the mass loss rate peak and the thermal kink to lower temperatures.

One hypothesis proposed herein to explain this phenomenon is the entrapment of liquid water at the innermost position of the sample. As the drying process progresses and the pressure at such positions decays, this trapped water at hot temperature can suddenly evaporate. This phase transition from liquid water to vapor can consume significant amounts of thermal energy, as seen by the comparison between the water heat of vaporization (which ranges from 2500 kJ/kg to 830kJ/kg between 0°C and 350°C [23]) and its specific heat (which ranges from 4.2 kJ/kg°C to 10kJ/kg°C between 0°C and 350°C [15]).

This entrapment and subsequent evaporation of liquid water may be responsible for the abrupt changes in the heating rate and the associated decrease in mass loss rate, generating the thermal kinks, as observed in Figure 6. The presence of polymeric fibers seems to influence this behavior, likely af-

fecting the water distribution and retention within the sample, which further impacts the thermal kink features.

Figure 7 shows a schematic representation of the proposed theory to explain the thermal kinks, considering a cross-section of a sample with $\ell =$ 30cm, equally heated from all sides for an idealized scenario. Steep thermal gradients are developed within the sample, as depicted in Figure 7 b), owing to the small Fourier number resulting in the formation of a ring of pressurization close to the sample's surface, described in Figure 7 c). As the pressure gradient within a porous media is inversely proportional to the mass flux (shown by Darcy's law), a mass flux towards both the environment and the center of the sample are generated. As a result, moisture accumulation at the innermost positions will happen, as described in Figure 7 d).

Under specific conditions, the pressurization at the center of the sample can sustain liquid water, even for temperatures well above the ebullition point at atmospheric pressures (consider that the pressurization ring formed in Figure 7 c) converges to the sample's center of mass). As the drying front reaches this position, and the pressure decays, the liquid water is suddenly vaporized, leading to the decrease of heating rate observed at the beginning of the thermal kink. Afterward, the reduced effective specific heat of this dried zone leads to the sharp increase in the heating rate until the dehydration reactions start to take place.

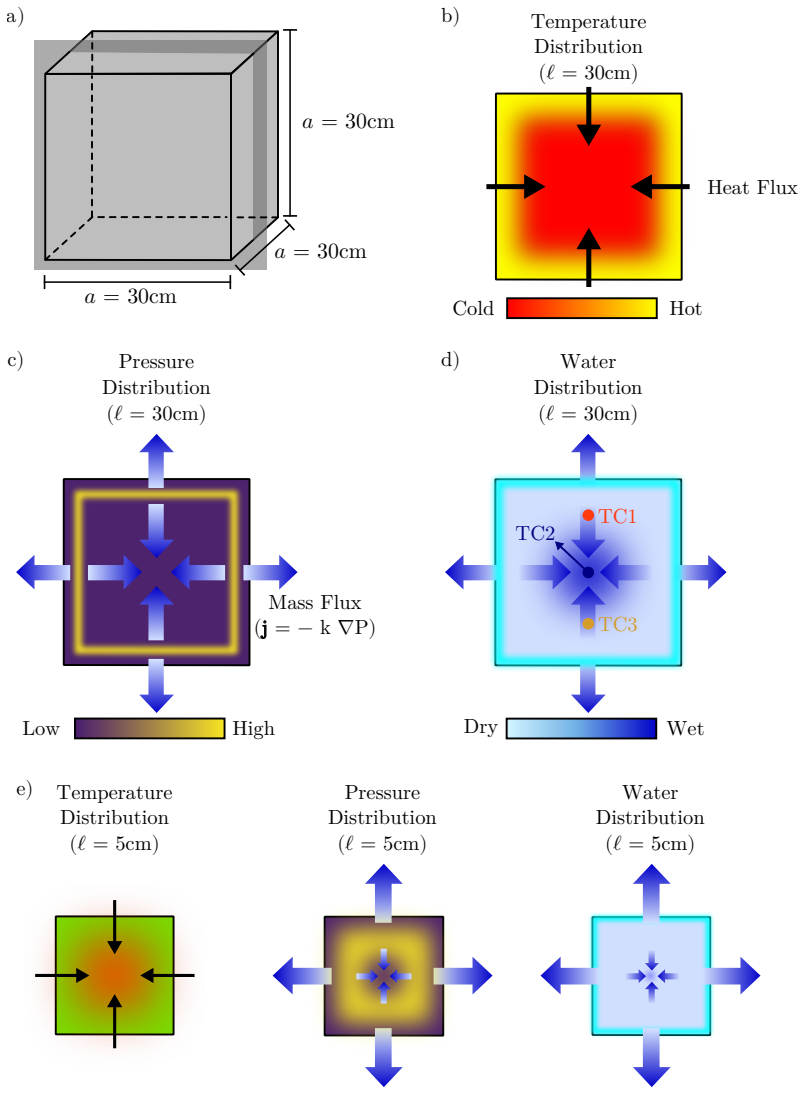


Figure 7: Theoretical framework for the explanation of the thermal kink on a section of the $\ell = 30cm$ sample (a), considering the temperature, (b), pressure, (c), and water distributions, (d). In (e), such quantities are represented for a smaller sample with $\ell = 5cm$, describing why the resulting temperature and pressure gradients do not lead to the intense moisture accumulation at the center of the sample.

Further investigation is needed to validate and fully understand this hypothesis, nonetheless, multiple observations in the literature can support this

conjecture: i) according to Auvray et al. [24] different hydrate types were detected among the phases formed during an explosion test of a calcium aluminate sample castable which were the products of a reaction that took place under hydrothermal conditions, suggesting the presence of an environment rich with pressurized water next to those specific regions.

Meanwhile, ii) Khoeller et al. [25] reported that during drying, hydrothermal conditions might occur, leading to changes in the phase composition and on the microstructure of the castables; and iii) Moreira et al. [26] used neutron tomography to prove that moisture accumulation occurs even for small samples (cylinders with 5cm in height and 3.6cm in diameter), by detecting an increase of water at the innermost positions of cylindrical samples.

Additionally, iv) Masara and co-authors used molecular dynamic simulations to investigate the role of thermal pressurization in concrete spalling, and it was found that for an undrained pore configuration, significant confining pressures (i.e. the pressure exerted by all the species present within the pores) were observed when the temperature was increased, whereas the simulation of a drained scenario with a constant vapor pressure showed even negative confining pressures at the smaller pores, due to the re-sorption of water molecules at the pore walls.

Furthermore, v), Innocentini et al. showed that when the heating rate applied in saturated samples during hot air permeability tests was increased from 1°C/min to 5°C/min, a severe thermal gradient between the input and output temperatures of the air was observed. This discrepancy arises due to the enthalpy of evaporation, causing the exit air temperature fixed at 100°C, while the inlet temperature increased up to 400°C [27].

Finally, vi) Felicetti et al. experimentally demonstrated that a sudden localized decrease in temperature can occur during quick depressurization of heated concrete pores. This finding further corroborates the close relationship between the physical state of water and its transitions with the thermal behavior of the sample.

To further illustrate the correlation between the water physical state and the drying, Figure 8 presents a panel with the phase diagram of water based on the Clausius-Clayperon relation [28], the derivative of the mass loss and the hydrates' decomposition, all as a function of the temperature.

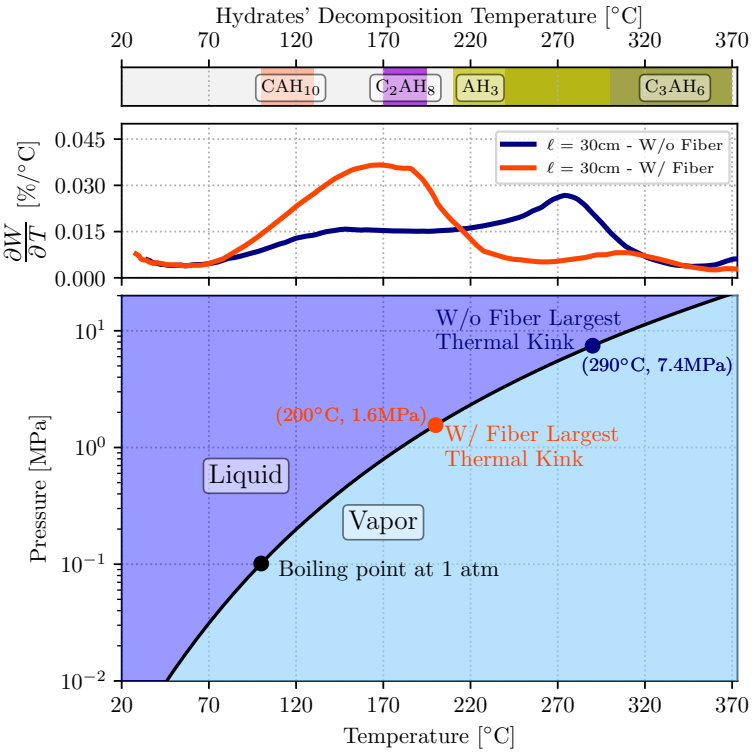


Figure 8: Phase diagram of water showing the locus of the first and most intense thermal kinks observed for the samples with and without polymeric fibers. A scale on the top of the phase diagram with the hydrates' decomposition temperature and the mass loss derivatives as a function of the sample temperature are also presented.

The temperature corresponding to the first and most intense thermal kink is highlighted by circular markers on the phase diagram (Figure 8), pointing out that the pressure required to maintain water in a liquid state at equilibrium within a closed system at the thermal kink temperature would be approximately 1.6 MPa for the sample with polymeric fibers and 7.4 MPa for the reference castable. These pressure levels could be reached during the drying of the castable, as shown by the pressure-temperature-mass (PTM) tests conducted by Fey et al. [29], where a maximum gas pressure of 1.8

MPa was measured for a composition with polymeric fibers heated at a rate of 0.93°C/min. Similar pressure levels were also reported by Meunier et al. [30].

It is worth mentioning that Dauti et al. reported on the potential for cracking Portland cement concrete samples during heating, even with the presence of thin thermocouples. This observation was carried out via neutron tomography [31], and it was attributed to thermal expansion mismatches between the metal and the ceramic. Thus, the local measurements obtained from PTM tests can be perceived as a lower bound estimate of the actual pressure values measured within a porous media without the cracks induced by these pressure probes.

Additionally, it is expected that in the absence of polymeric fibers, the maximum pressure levels observed during drying will be higher when compared to the compositions containing them. This is attributed to the lower intrinsic permeability of the reference material. Moreover, the shift of the mass release rate to higher temperatures, as depicted in Figure 8, implies the presence of water vapor at high pressures at such a condition. This can be assessed when considering Anthoine's semi-empirical law, in which the water vapor pressure exponentially increases with temperature. This also helps to shift the thermal kink observed in the reference composition to higher temperatures and pressures, as observed by the dark blue markers added to the water phase diagram.

Another noteworthy observation derived from the diagram in Figure 8 is that the thermal kinks occur precisely within the temperature ranges associated with the hydrates' decomposition reactions for the phases commonly

present in cured calcium aluminate cement castables [4, 5]. For instance, the thermal kink for the 5CAC-ED composition aligns with the window of thermal dehydration for the $C_2AH_8$ phase, whereas for the 5CAC one, it coincides with the intersection of the decomposition of $AH_3$ and $C_3AH_6$ phases. The second kinks (not highlighted in Figure 8) would lie in the range of the decomposition of the $C_3AH_6$ phase.

These reactions act as supplementary water sources, and they can lead to an increase in water molecules within the pores of the castable under critical conditions required for the thermal kinks to occur. As these reactions take place, the vapor buildup within the pores stops and the rate of mass release begins to decline. Consequently, the local pressure at the center of the sample diminishes, dictating the rapid evaporation of liquid water, in line with the theory proposed in this study to explain the thermal kinks.

The sudden release of water molecules during dehydration can also induce a re-pressurization of the gas within the pores, providing a plausible explanation for the second kink to occur, observed at higher temperatures.

It should be noted that the mere existence of this size dependent phenomena is crucial, as it underscores that relying solely on conventional thermogravimetry with small-sized samples can overlook crucial phenomena that are determinant for the drying of larger bodies.

To elucidate why the thermal kink is absent in smaller samples, Figure 7 e) shows that when the characteristic length is reduced (i.e. considering sample with $\ell$ =5cm), the thermal gradients become less steep, resulting in a more uniform pressure distribution. Consequently, there is a reduced accumulation of water at the center of the sample. Moreover, the higher surface area

to volume ratio ensures that the moisture flux towards the environment is considerably higher compared to the ones in the direction of the sample's center of mass.

Thus, considering the proposed mechanism for explaining the thermal kink presence, the behavior of all the different samples can be compared based on a normalized sample heating rate, $\dot{\theta}$, which is the ratio between the derivative of the temperature evolution measured at the center of the sample ($\frac{dT_s}{dt}$) and the heating rate applied during the test ($\dot{T_h}$), as depicted in Figure 9. This quantity is computed to facilitate the direct comparison between the samples subjected to varying imposed heating rates. Equation 4 describes how $\dot{\theta}$ is calculated.

$$\dot{\theta} = \frac{\frac{dT_s}{dt}}{\dot{T_h}} \tag{4}$$

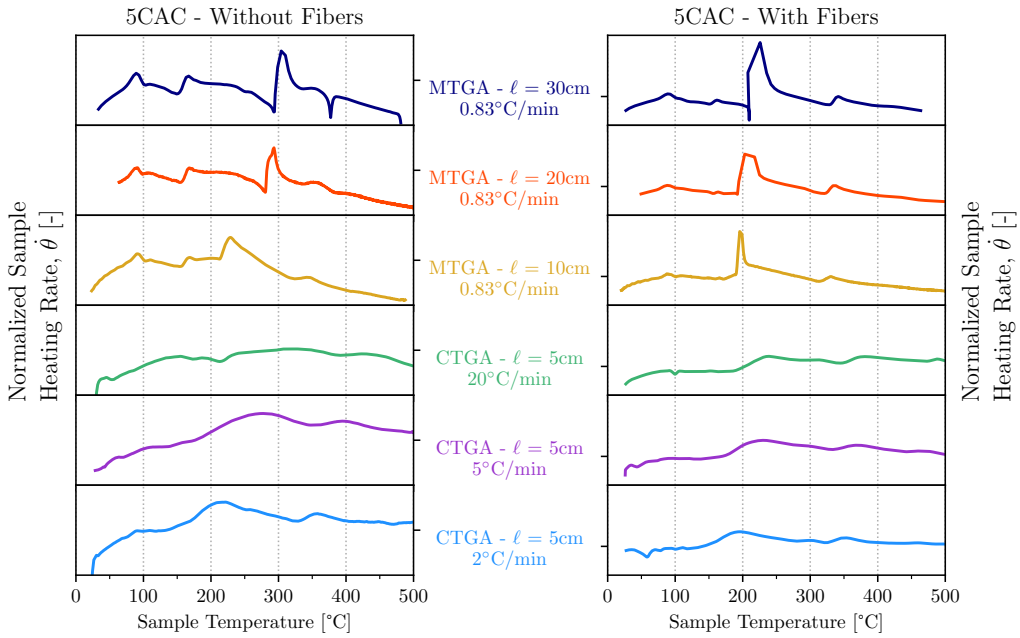


Figure 9: Normalized sample heating rate as a function of the sample temperature for compositions without (left column) and with polymeric fibers (right column) for all different characteristic lengths ($\ell$) investigated in this work. MTGA: Macro thermogravimetry, CTGA: Conventional thermogravimetry.

The thermal kink is readily identified by the abrupt change in the normalized sample heating rate. Notably, the intensity of this phenomenon presents a direct correlation with the sample size for the MTGA experiments. For samples without polymeric fibers, this behavior is observed for the different range of sizes, indicating a clear scale effect not clearly seen for the fiber-containing compositions.

Moreover, when attempting to induce a higher thermal gradient by increasing the heating rate for the CTGA test, which would perhaps better match those observed for larger MTGA samples, no thermal kinks were observed (as seen for the bottom three rows in Figure 9). In fact, for the 5CAC

composition, the normalized heating rate of the sample with a closer profile to that observed for the larger MTGA test was attained using a heating rate of 2°C/min. In parallel to the findings for the size effect on the fiber-containing composition, the incorporation of this additive also led to a dampened effect of the heating rate on the curves of the normalized sample heating rate.

To investigate the impact of various factors, including sample sizes, heating rates, and the presence of polymeric fibers, on the drying dynamics of the samples, the mass loss for both reference compositions and those containing polymeric fibers is depicted in Figure 10.

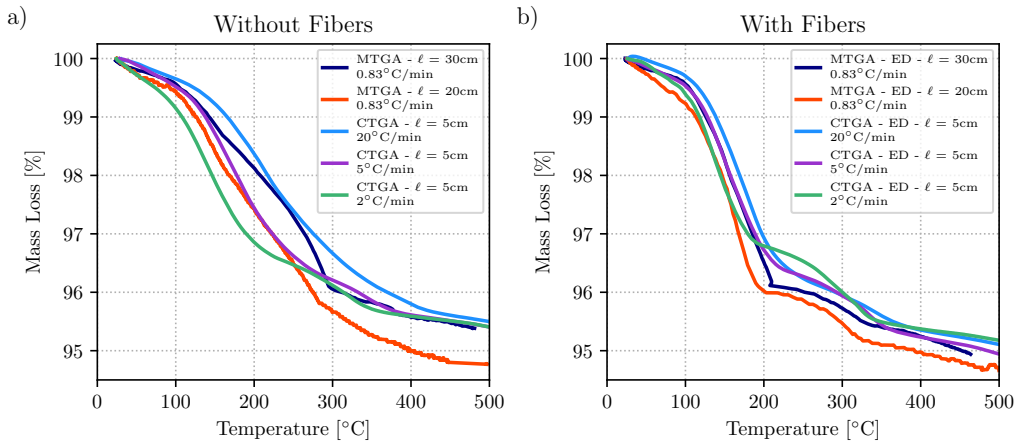


Figure 10: Mass loss for compositions without, (a), and with polymeric fibers, (b) for the samples with characteristic sizes, $\ell = 30$cm, $\ell = 20$cm and $\ell = 5$cm.

A noticeable trend can be observed for the composition without fibers, where the drying process gradually shifts to higher temperatures with an increase in either the sample size or the heating rate. However, it is important to acknowledge that the mass loss of the sample with $\ell = 20$ cm is slightly overestimated as the total water content is 5% wt., while the total mass loss was roughly 5.2 % wt. This discrepancy is attributed to the MTGA system,

originally designed for larger samples. Hence, this latter effect and the noisier resulted signal was also the reason for not including the mass loss results for samples with a characteristic length $\ell = 10$ cm.

Moreover, it is clear that the initial stages of the mass loss of the sample with $\ell = 30$cm resembles the behavior observed for the CTGA test with a heating rate of 20°C/min, whereas the sample with a characteristic length of 20 cm shows similarities with the CTGA test conducted at 5°C/min. This observation emphasizes that the more comparable thermal states, as indicated by the Fourier number shown in Figure 2, result in more similar mass loss behaviors during the initial stages of drying, specifically during evaporation (25°- 100°) and ebullition (100°- 300°).

Meanwhile, the dehydration stage of the drying is characterized by thermoactivated transitions that are highly dependent of the heating rate [4, 5]. As a consequence, the mass loss observed at higher temperatures for the sample with a characteristic length of 30 cm is better represented by the CTGA tests with smaller heating rates (5°C/min and 2°C/min).

When analyzing the composition containing polymeric fibers, the spread of the results is significantly reduced, which is linked to the closer normalized sample heating rates values for these compositions (Figure 9).

As the 5CAC-ED composition presents higher intrinsic permeability after 100°C due to the fiber melting [22], the water can be more easily released even when its path from the samples' center to its surface is increased for the larger samples. Therefore, it is still possible to withdraw the releasing vapor at similar rates than the ones observed for the smaller samples. For a more detailed analysis of the water removal dynamics, Figure 11 illustrates

the derivative of the mass with respect to the samples' temperatures.

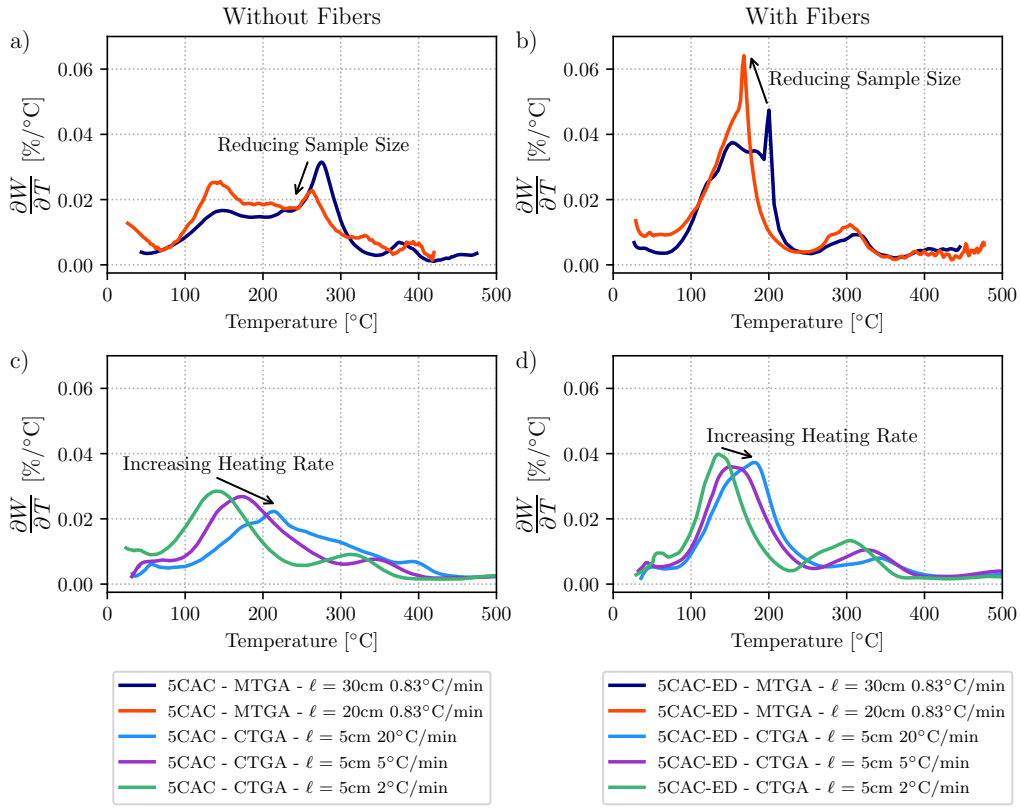


Figure 11: Mass loss derivatives with respect to the sample's temperature for compositions without, (a) and (c), and with polymeric fibers, (b) and (d).

The impact of reducing the sample size for compositions without drying additives (Figure 11 a) becomes evident as it shifts the position of the highest water removal peak towards lower temperatures. For the $\ell$=30cm sample, the peak occurs around 280 °C, whereas for the $\ell$=20cm sample, the maximum water removal rate takes place at approximately 130°C. This change is attributed to the greater difficulty that the hot water vapor faces to be released from the larger body, primarily due to the longer path it must cross

to reach the surface and also because of its smaller surface area to volume ratio.

The influence of the heating rate on the 5CAC-ED composition is also evident, although the derivative of the mass loss with respect to the temperature is closer for the samples with distinct sizes and the peak shifts within a narrower temperature range. Furthermore, it is important to highlight that for the 5CAC, the highest water removal rate is observed for the sample with a characteristic length of $\ell$ = 30cm (Figure 11 a)), whereas for the fiber-containing samples, the peak shift towards lower temperatures is coupled to an increase in the maximum mass loss rate (Figure 11 b)).

As previously discussed, the increase in the heating rate resulted in a displacement of the mass loss peaks towards higher temperatures associated with the dehydration reactions, as depicted in Figures 11 c) and d). This upward translation also affected the initial peaks of mass loss linked to the ebullition stage of drying. However, it is again noteworthy that the presence of fibers mitigates the impact of both the sample size and heating rate on these drying dynamics.

## 4. Conclusions

The size effect on the drying dynamics of refractory castables under different conditions was investigated in this study. Various combinations of sample geometries and heating rates yielded distinct Fourier numbers, which highlighted the changes on the thermal state of the bodies during these thermogravimetry tests. Furthermore, the presence of polymeric fibers were also evaluated.

Upon closer inspection of the thermal evolution of the samples, the presence of a thermal kink phenomenon was observed for the larger samples (i.e. those with characteristic length $\ell \geq 10$cm). This took place at specific positions in the center of the sample and within a narrow range of temperatures, regardless of the Macro TGA sample's dimensions. However, the intensity of this physical process, characterized by an abrupt change in the normalized sample heating rate, was directly proportional to the sample size.

It was hypothesized that this process can be explained by the rapid vaporization of liquid water, which accumulates at the center of the sample and is sustained as a liquid due to the high pressures within the pores. As the castable undergoes drying and the pressurization decreases, the equilibrium state of water at this novel condition shifts from liquid to vapor, resulting in a phase transition that consumes a significant portion of the energy provided during the castable's heating.

As the sample size is decreased, the thermal gradients are reduced, resulting in a smaller region within the body where the pressure peaks (which are also less intense) were detected. This reduces the amount of water accumulated inside the sample, generating conditions in which the abrupt vaporization of water does not significantly affect the thermal readings at the center of the sample. Consequently, no thermal kinks were observed for the smaller samples tested with the conventional TGA equipment, even when the heating rate was increased to induce smaller Fourier numbers and larger thermal gradients.

Significant variations in mass loss behavior during drying were found out based on sample size and heating rate for compositions without drying addi-

tives. Conversely, the influence of sample size and heating rate on mass loss behavior was reduced in the presence of polymeric fibers. Moreover, dehydration reactions during drying were highly dependent on the heating rate, leading to shifts in the largest water removal peaks to higher temperatures with increasing heating rate. Nevertheless, the presence of fibers mitigated these effects, resulting in more similar profiles and less significant peak shifts.

The importance of considering the size of the refractory castable samples tested on the drying dynamics effects was highlighted by the findings attained in this study. Size-dependent phenomena, exemplified by the thermal kinks identified on the heating curves at the center of the larger samples, suggested the need of suitable experimental setups and heating rates to ensure accurate analysis of the process that takes place at the industrial equipment.

Finally, the framework proposed herein provides a reliable approach to investigate the effect of different sizes on the drying of castables inducing a better approximation between the industrial reality and the laboratory experimentation. Nevertheless, further studies are required to reveal semi-empirical general laws that could be useful as helpful guidelines for the design of safe and efficient drying procedures at real structure scales, similar to what has been carried out in the recent advancements to understand the mechanical size effect in civil engineering area.

## 5. Acknowledgments

This study was financed in part by the Coordenação de Aperfeiçoamento de Pessoal de Nível Superior - Brasil (CAPES) - Finance Code 001 and the ANR (Agence Nationale pour la Recherche) MULTI-FIRE. The authors

would like to thank the Fundação de Amparo à Pesquisa do Estado de São Paulo - FAPESP (grant number: 2021/00251-0). Finally, the authors are thankful for FIRE support to carry out this work.

## References


[1] C. R. Gagg, Cement and concrete as an engineering material: An historic appraisal and case study analysis, Engineering Failure Analysis 40 (2014) 114–140.

[2] C. Schacht, Refractories Handbook, Mechanical engineering, CRC Press, 2004.

[3] D. Kujanen, Technical ceramics and refractories applications and volumes literature review, Bachelor's thesis, Tampere University, 2019.

[4] A. P. da Luz, M. A. L. Braulio, V. C. Pandolfelli, Refractory castable engineering, Goller Verlag GmbH, Baden-Baden, 2015, pp. 331–334.

[5] A. P. Luz, M. H. Moreira, M. A. L. Braulio, C. Parr, V. C. Pandolfelli, Drying behavior of dense refractory ceramic castables. part 1–general aspects and experimental techniques used to assess water removal, Ceramics International 47 (2021) 22246–22268.

[6] R. Jansson, Fire spalling of concrete: theoretical and experimental studies, Ph.D. thesis, KTH Royal Institute of Technology, 2013.

[7] M. H. Moreira, S. Dal Pont, R. F. Ausas, A. P. Luz, T. M. Cunha, C. Parr, V. C. Pandolfelli, Main trends on the simulation of the drying of refractory castables-Review, Ceramics International 47 (2021) 28086–28105.

[8] M. Ozawa, S. Uchida, T. Kamada, H. Morimoto, Study of mechanisms of explosive spalling in high-strength concrete at high temperatures using

acoustic emission, Construction and Building Materials 37 (2012) 621–628. doi:10.1016/j.conbuildmat.2012.06.070.

[9] G. Palmer, J. Cobos, T. Howes, The accelerated drying of refractory concrete - part 1 : A review of current understanding, Refractories Worldforum 6 (2014) 75–83.

[10] Z. P. Bažant, Scaling theory for quasibrittle structural failure, Proceedings of the National Academy of Sciences 101 (2004) 13400–13407.

[11] W. Weibull, A statistical distribution function of wide applicability, Journal of Applied Mechanics 18 (1951) 293–297.

[12] L. Alarcon-Ruiz, M. Brocato, S. Dal Pont, A. Feraille, Size effect in concrete intrinsic permeability measurements, Transport in Porous Media 85 (2010) 541–564.

[13] S. J. Lukasiewicz, Spray-drying ceramic powders, Journal of the American Ceramic Society 72 (1989) 617–624.

[14] F. Cardoso, M. Innocentini, M. Akiyoshi, L. Bittencourt, V. Pandolfelli, Scale-up effect on the drying behavior of high-alumina refractory castables, Taikabutsu Overseas 23 (2003) 226–230.

[15] F. P. Incropera, D. P. DeWitt, T. L. Bergman, A. S. Lavine, et al., Fundamentals of Heat and Mass Transfer, volume 6, Wiley New York, 1996.

[16] R. J. Connolly, The spalling of concrete in fires., Ph.D. thesis, Aston University Birmingham, 1995.

[17] R. Jansson, L. Boström, Factors influencing fire spalling of self compacting concrete, Materials and Structures 46 (2013) 1683–1694.

[18] V. K. R. Kodur, Fire performance of high-strength concrete structural members, Construction Technology Updates 31 (1999).

[19] L. Boström, U. Wickström, B. Adl-Zarrabi, Effect of specimen size and loading conditions on spalling of concrete, Fire and Materials: An International Journal 31 (2007) 173–186.

[20] A. Mohd Ali, J. Sanjayan, M. Guerrieri, Specimens size, aggregate size, and aggregate type effect on spalling of concrete in fire, Fire and Materials 42 (2018) 59–68.

[21] F. Sultangaliyeva, H. Carré, C. La Borderie, F. Robert, S. Mohaine, P. Pimienta, Scale effect on spalling of high performance self-compacting fiber reinforced concrete, in: 7th International Workshop on Concrete Spalling due to Fire Exposure, 2022.

[22] H. Peng, B. Myhre, Improved explosion resistance of low cement refractory castables using drying agents, International Journal of Ceramic Engineering & Science 4 (2022) 84–91.

[23] B. Henderson-Sellers, A new formula for latent heat of vaporization of water as a function of temperature, Quarterly Journal of the Royal Meteorological Society 110 (1984) 1186–1190.

[24] J. Auvray, C. Zetterström, C. Wöhrmeyer, H. Fryda, C. Parr, C. Eychenne-Baron, Dry-out simulation of castables containing calcium

aluminate cement under hydrothermal conditions, in: Proceedings of the Unified International Technical Conference on Refractories (UNITECR 2013), John Wiley & Sons, 2014, p. 159.

[25] A. Koehler, C. Rößler, J. Neubauer, F. Goetz-Neunhoeffer, Phase and porosity changes in a calcium aluminate cement and alumina system under hydrothermal conditions, Ceramics International 49 (2023) 4659–4667.

[26] M. H. Moreira, S. Dal Pont, A. Tengattini, A. P. Luz, V. C. Pandolfelli, Experimental proof of moisture clog through neutron tomography in a porous medium under truly one-directional drying, Journal of the American Ceramic Society 105 (2022) 3534–3543.

[27] M. D. Innocentini, C. Ribeiro, L. R. Bittencourt, V. C. Pandolfelli, Fluid dynamics and thermal aspects of the dewatering of high-alumina refractory castables: Removal of physically absorbed water, Journal of the American Ceramic Society 84 (2001) 2696–2698.

[28] R. DeHoff, Thermodynamics in materials science, CRC Press, 2006.

[29] K. G. Fey, I. Riehl, R. Wulf, U. Gross, Experimental and numerical investigation of the first heat-up of refractory concrete, International Journal of Thermal Sciences 100 (2016) 108–125.

[30] P. Meunier, J. Mindeguia, P. Pimienta, Mass, temperature and pressure measurements during the dry out of refractory castables, in: 51st International Colloquium on Refractories, 2008, pp. 95–98.

[31] D. Dauti, A. Tengattini, S. Dal Pont, N. Toropovs, M. Briffaut, B. Weber, Some observations on testing conditions of high-temperature experiments on concrete: An insight from neutron tomography, Transport in Porous Media (2020) 1–12.